Expected performance of missing transverse momentum reconstruction for the ATLAS detector at $\sqrt{s} = 13$ TeV

The ATLAS Collaboration

Abstract

This document summarises the expected performance of the missing transverse momentum reconstruction for early Run 2 data in the ATLAS detector. The performance of the missing transverse momentum reconstruction is evaluated using Monte Carlo simulations of proton-proton collisions at a centre-of-mass energy of 13 TeV. Different missing transverse momentum definitions using calorimeter energy deposits and tracks reconstructed by the ATLAS Inner Detector are compared in a variety of event topologies. Estimates of the systematic uncertainty on measurements of $E_{\mathrm{T}}^{\mathrm{miss}}$ are described.

1 Introduction

During 2015, the Large Hadron Collider (LHC) began proton-proton collisions at a 13 TeV centre-of-mass energy. This higher energy, together with an increased luminosity, offers prospects for refining precision measurements and extending the reach of previous searches for Beyond the Standard Model (BSM) signatures. During the period of LHC shut-down, significant effort was devoted to estimating the performance of the ATLAS detector under these new conditions, based on Monte Carlo simulations and Run 1 experience. This document addresses the reconstruction of missing transverse momentum and its expected performance in Run 2.

Conservation of momentum in the plane transverse to the beam axis implies that the vector transverse momenta of the collision products should sum to zero. An imbalance in the sum of visible transverse momenta is known as "missing transverse momentum", or E_T^{miss}. This may be indicative of weakly-interacting, stable particles in the final state. Within the Standard Model, these particles are the neutrinos. There are also prospects for such particles in theories beyond the Standard Model, making E_T^{miss} an important variable in searches. The measurement of E_T^{miss} is affected by interacting Standard Model particles which are poorly reconstructed, escape the acceptance of the detector or otherwise fail to be reconstructed altogether. The missing transverse momentum thus also serves as an important measure of the performance of the detector and the event reconstruction process. Several algorithms have been developed to quantify the missing transverse momentum. The study presented here compares three of these: CST E_T^{miss} [1–4], Track E_T^{miss} and TST E_T^{miss}.

CST E_T^{miss} is a method based on energy deposits in the ATLAS calorimeters. This includes a calorimeter-based soft term (CST), which is constructed from the energy deposits in the calorimeter not associated with hard objects: selected and reconstructed electrons, photons, hadronically decaying tau-leptons, muons or jets. Contributions to the soft term arise from underlying event activity and soft radiation from the hard event.

One of the weaknesses of the calorimeter-based approach is its vulnerability to additional proton-proton interactions overlapping the hard-scatter process (pile-up interactions). These interactions, which can happen in the same bunch crossing (in-time pile-up) or in neighbouring bunch crossings (out-of-time pile-up) [5], give an additional contribution to the calorimeter-based soft term.

Inner Detector[1] (ID) tracks may be associated to vertices, and so to a particular pp collision. Track-based methods therefore offer greater resilience under the conditions of increased pile-up expected during Run 2. Track E_T^{miss} is an E_T^{miss} definition based on the momenta of ID tracks, a measure which is largely independent of the pile-up. A purely track-based quantity is, however, insensitive to neutral particles (which do not leave tracks in the ID) and has an acceptance limited by the tracking volume of the ATLAS tracker. TST E_T^{miss} uses a track-based soft term (TST), but combines this with calorimeter-based measurements for the hard objects. This presents a good compromise between the calorimeter- and track-based approaches, and is the primary method of E_T^{miss} reconstruction in Run 2.

The performance of the E_T^{miss} algorithms described above is evaluated using Monte Carlo simulations of several processes. These are chosen for characteristics which together give a complete picture of E_T^{miss} performance. The $Z \rightarrow \ell\ell$ process, with $\ell\ell$ being an electron-positron or muon-antimuon pair, is the standard for the evaluation of E_T^{miss} performance owing to its clean detector signature. These events have very little "genuine" transverse missing momentum. The reconstructed E_T^{miss} in $Z \rightarrow \mu\mu$ events therefore

---

[1] Section 2 gives a brief description of the ID. For an exhaustive description, see the references in that section.

gives information about the intrinsic resolution of the detector, of the algorithms involved and of the object reconstruction efficiencies. $W \rightarrow \ell\nu$ events provide a topology with high-p_T neutrinos, in which E_T^{miss} is expected to be non-zero. These therefore give information on the scale of E_T^{miss}. Top-antitop pair ($t\bar{t}$) events provide a topology with many jets, and so are useful in investigating the robustness of E_T^{miss} reconstruction in multijet environments.

This note is organised as follows. Section 2 gives a brief description of the ATLAS detector. Section 3 describes the Monte Carlo simulation samples used in this analysis, and Section 4 the object selections applied. Section 5 gives more detail on the reconstruction of E_T^{miss}, and presents the jet selection used. The selections applied for each of the event topologies used in the performance study are described in Section 6. Section 7 examines the characteristics and performance of CST E_T^{miss}, TST E_T^{miss} and Track E_T^{miss}. Section 8 discusses the method and results of a study to estimate the systematic uncertainties in the TST E_T^{miss} algorithm, and the additional contribution needed for Track E_T^{miss}. Studies of the systematic uncertainties in the CST are not presented here.

2 The ATLAS detector

The ATLAS experiment [6] is a multi-purpose particle detector with a forward-backward symmetric cylindrical geometry and near 4π coverage in solid angle[2]. It consists of an inner tracking detector (ID) surrounded by a thin superconducting solenoid providing a 2 T axial magnetic field, electromagnetic and hadronic calorimeters, and a muon spectrometer (MS). The ID covers the pseudorapidity range $|\eta| < 2.5$, and consists of a silicon pixel detector, a silicon micro-strip detector (SCT), and, for $|\eta| < 2.0$, a transition radiation tracker (TRT). During the first long shutdown (LS1), a new tracking layer, known as the Insertable B-Layer (IBL) [7], was added close to the beam pipe. A high-granularity lead/liquid-argon (LAr) sampling electromagnetic calorimeter covers the region $|\eta| < 3.2$. An iron/scintillator-tile calorimeter provides hadronic coverage in the central pseudorapidity range $|\eta| < 1.7$. LAr technology is also used for the hadronic calorimeters in the end-cap region $1.5 < |\eta| < 3.2$ and for both electromagnetic and hadronic measurements in the forward region up to $|\eta| < 4.9$. The MS surrounds the calorimeters. It consists of three large air-core superconducting toroidal magnet systems, precision tracking chambers providing accurate muon tracking out to $|\eta| = 2.7$, and additional detectors for triggering in the region $|\eta| < 2.4$. A first-level hardware trigger and a higher-level software trigger [8] are used to select events for analysis.

3 Monte Carlo simulation samples

The performance studies are based on $Z \rightarrow \ell\ell$, $W \rightarrow \ell\nu$ and $t\bar{t}$ Monte Carlo (MC) simulated events. The $Z \rightarrow \ell\ell$ and $W \rightarrow \ell\nu$ samples were generated by POWHEG [9] interfaced to PYTHIA8 [10]. POWHEG is a method for the implementation of corrections up to next-to-leading order in α_S (NLO). PYTHIA uses p_T-ordered parton showering and a string hadronisation scheme to model the complete evolution of the

---

[2] ATLAS uses a right-handed coordinate system with its origin at the nominal interaction point (IP) in the centre of the detector and the z-axis along the beam pipe. The x-axis points from the IP to the centre of the LHC ring, and the y-axis points upwards. Cylindrical coordinates (r, ϕ) are used in the transverse plane, ϕ being the azimuthal angle around the z-axis. The pseudorapidity is defined in terms of the polar angle θ as $\eta = -\ln\tan(\theta/2)$. Angular distance is measured in units of $\Delta R \equiv \sqrt{(\Delta\eta)^2 + (\Delta\phi)^2}$.
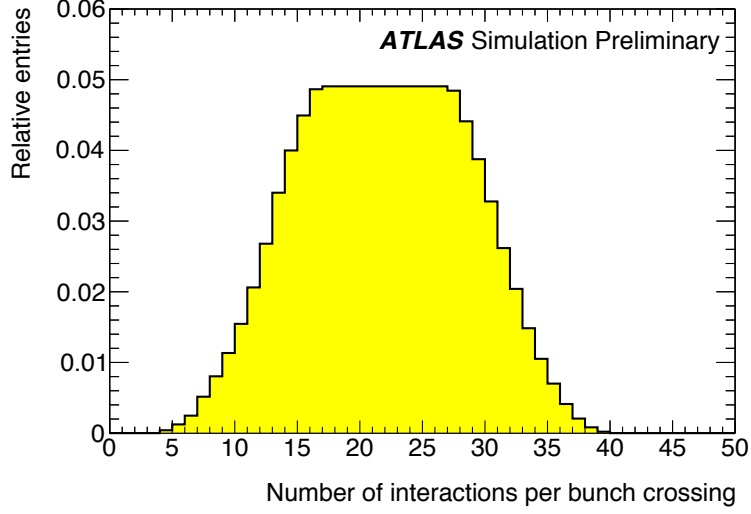
Figure 1: The distribution of the average number of interactions per bunch crossing $\langle\mu\rangle$ as assumed in the simulated samples used in this study.

interaction. For the $Z \to \ell\ell$ and $W \to \ell\nu$ samples, the CT10 [11] PDF set is used in the matrix element. The AZNLO [12] tune is used with the CTEQ6L1 [13] PDF set for the modelling of non-perturbative effects. The $t\bar{t}$ sample used Powheg interfaced to Pythia6 [14] and the PERUGIA2012 [15] tune. The matrix-element-level Monte Carlo calculations are matched to a model of the parton shower, the underlying event, and hadronisation [16–18]. After generating to a stable particle level, the events are processed using a Geant 4-based [19] full simulation of the ATLAS detector [20].

The systematic uncertainties in E_T^{miss} are estimated by the comparison of the "nominal" Powheg+Pythia8 sample with several alternative event generators and parton shower models. The Sherpa [21] and Herwig++ [22] generators are considered as alternatives. Sherpa is a multi-leg generator that computes up to five additional partons at tree level. Herwig++ is a general-purpose event generator using a cluster hadronisation model. The Sherpa and Herwig samples use PDFs from the CT10 [11] and CTEQ6L1 sets respectively. A comparison is also made between the predictions of the ATLAS detector simulation using Geant4 and a fast simulation model [23] which parametrises phenomena such as the development of hadronic showers in the calorimeter. Additional checks have been made with an alternative detector geometry, which allows the study of the impact of potential distortions in the detector material distribution.

The pile-up collisions are generated with Pythia8 using the MSTW2008 LO PDF [24] and the ATLAS A2 tune [25]. Pile-up interactions are overlaid on the hard-scatter events before event reconstruction. The number of additional pp collisions per bunch crossing to apply is drawn from a Poisson distribution of the average number of interactions per bunch crossing μ. The distribution of $\langle\mu\rangle$ assumed in the samples used in this study is shown in Fig. 1. The samples are overlaid assuming a 25 ns bunch spacing, as is planned for the majority of Run 2 data-taking. Some dedicated samples with 50 ns bunch spacing have been studied in order to investigate the effect of this variation, which will be used during the first period of data-taking.

4 Object selection

Analysis-dependent pre-selections are applied to the reconstructed candidates for electrons, muons, photons and hadronically decaying tau-leptons. Prompt tau-leptons and photons are not expected in $Z \to \mu\mu$ events. Taus and photons are included in the object selection, however, in order to study cases in which jets are falsely reconstructed. The fake hadronically decaying tau-leptons and photons may have a significant effect in other topologies.

The remainder of this section describes the selections made for reconstructed electrons, muons, photons and hadronically decaying tau-leptons. The software framework developed to reconstruct the $E_{\mathrm{T}}^{\mathrm{miss}}$ permits complete flexibility in these selections, which may be chosen to suit the needs of each analysis. The requirements made of the jets are recorded separately in Section 5.1, since their selection is part of the performance optimisation of $E_{\mathrm{T}}^{\mathrm{miss}}$, and an explicit selection for $E_{\mathrm{T}}^{\mathrm{miss}}$ reconstruction is made.

4.1 Track selection

The ATLAS detector measures charged particle momenta using the ID [26]. The series of energy deposits ("hits") in the ID are reconstructed as tracks [27] and the proton-proton collisions producing multiple tracks are reconstructed into vertices [28].

In order to ensure the quality of the tracks which are used to reconstruct the $E_{\mathrm{T}}^{\mathrm{miss}}$, a number of criteria must be met. Tracks must have a reconstructed p_{T} of 0.5 GeV or greater, and lie within the acceptance of the ID ($|\eta| < 2.5$). Requirements on the number of hits in each layer of the ID ensure that the track p_{T} is accurately calculated by the reconstruction. These follow the recommendations of the tracking performance group, requiring at least 7 hits in the silicon detector and no more than two holes in the silicon layers or one hole in the pixel layers.

The primary vertex (PV) in each event is the vertex with the largest value of Σp_{T}^2, where the scalar sum is taken over all the tracks associated with that vertex during reconstruction. To ensure the reconstructed vertex is consistent with the track geometry, it is required that the transverse impact parameter (d_0) be less than 1.5 mm. This is the particle's distance of closest approach to the primary vertex in the plane transverse to the beam-line. It is also required that the d_0 significance, $d_0/\sigma(d_0)$, be less than 3. The PV corresponds to the vertex of the hard scatter interaction to a very high efficiency.

4.2 Muon selection

Muons are selected for this analysis according to criteria similar to those used during Run 1 [29]. Muons with $|\eta| < 2.5$ are required to be reconstructed in the MS with a matching track in the ID. Those muon candidates with a large imbalance between the momentum measured by the ID and by the MS are rejected, as these typically result from in-flight decay of light mesons. The acceptance is extended to cover the range $2.5 < |\eta| < 2.7$ by allowing muons reconstructed in the MS only, but with tightened requirements on the number of MS track hits. In addition, muons are required to have p_{T} greater than 10 GeV.

4.3 Electron selection

Electrons are reconstructed from clusters in the electromagnetic calorimeter associated with ID tracks [30]. The identification of electrons is performed using a likelihood-based criterion [31]. For this analysis, the threshold is set at the "Medium" working point. Electrons are required to fall within $|\eta| < 2.47$ and to have p_T greater than 10 GeV. Those falling within the transition region between the barrel and end-cap electromagnetic calorimeters, $1.37 < |\eta| < 1.52$, are not considered. Electron momentum is measured following the strategy detailed in Ref. [30].

4.4 Photon selection

Photon identification exploits the different evolution of the electromagnetic showers resulting from photons and from jets [32]. This is implemented using a set of orthogonal requirements on the shower shape. The "Tight" working point is used, which provides a high rejection of fake photons arising from neutral meson decays. Additionally, photons must have a calibrated p_T greater than 25 GeV and $|\eta| < 2.37$. Photons falling within the the transition region between the barrel and end-cap electromagnetic calorimeters, $1.37 < |\eta| < 1.52$, are poorly measured and so are discarded.

4.5 Tau selection

Hadronically decaying tau-leptons may be differentiated from jets based on their low track-multiplicity and narrow shower shape. These and other discriminating characteristics are combined in a Boosted Decision Tree. This analysis uses the "Medium" working point, as described in Ref. [33]. Additionally, hadronically decaying tau-leptons are required to have $p_T > 20$ GeV and $|\eta| < 2.5$. Tau jet candidates falling within the the transition region between the barrel and end-cap electromagnetic calorimeters, $1.37 < |\eta| < 1.52$, are not considered.

5 E_T^{miss} definition and reconstruction

The E_T^{miss} reconstruction process uses reconstructed, calibrated objects to estimate the transverse momentum imbalance in an event. The E_T^{miss} of an event is calculated as the sum of a number of components:

$$E_{x(y)}^{\text{miss}} = E_{x(y)}^{\text{miss},\, e} + E_{x(y)}^{\text{miss},\, \gamma} + E_{x(y)}^{\text{miss},\, \tau} + E_{x(y)}^{\text{miss, jets}} + E_{x(y)}^{\text{miss},\, \mu} + E_{x(y)}^{\text{miss, soft}} . \tag{1}$$

The terms for jets, charged leptons, and photons are the negative sum of the momenta for the respective calibrated objects. Calorimeter deposits are associated with reconstructed objects in the following order: electrons (e), photons (γ), hadronically decaying tau-leptons (τ), jets, and finally muons (μ).

The "soft" term is reconstructed from the transverse momentum deposited in the detector but not associated with any reconstructed hard object (electron, photon, hadronically-decaying tau-lepton, jet or muon). It may be reconstructed either by calorimeter-based methods, known as the Calorimeter Soft Term (CST), or track-based methods, resulting in the Track Soft Term (TST). The choice of soft-term algorithm influences the performance of and uncertainties in E_T^{miss} reconstruction.

From the components $E^{\text{miss}}_{x(y)}$, the magnitude $E^{\text{miss}}_{\text{T}}$ and azimuthal angle ϕ^{miss} are calculated as

$$E^{\text{miss}}_{\text{T}} = \sqrt{\left(E^{\text{miss}}_x\right)^2 + \left(E^{\text{miss}}_y\right)^2} \,, \tag{2}$$

$$\phi^{\text{miss}} = \arctan\left(E^{\text{miss}}_y / E^{\text{miss}}_x\right) \,. \tag{3}$$

The total transverse energy in the event, $\sum E_{\text{T}}$, is used to quantify the event activity. It is defined as the scalar sum of transverse momenta of the objects used to calculate the $E^{\text{miss}}_{\text{T}}$:

$$\sum E_{\text{T}} = \sum p^e_{\text{T}} + \sum p^\gamma_{\text{T}} + \sum p^\tau_{\text{T}} + \sum p^{\text{jets}}_{\text{T}} + \sum p^\mu_{\text{T}} + \sum p^{\text{soft}}_{\text{T}}. \tag{4}$$

The objects contributing to the electron, muon, tau and photon terms in Eq. 1 are selected as appropriate for a given analysis. Those selections used for this performance study are described in Section 4. For the objects used in the $E^{\text{miss}}_{\text{T}}$ jet term reconstruction, an explicit selection is made. This is outlined in the following section.

5.1 Jet selection

To suppress noise, calorimeter cell energy measurements are grouped into three-dimensional topological clusters ("topoclusters") [34]. Jets are reconstructed from topoclusters using the anti-k_t algorithm [35] with distance parameter $R = 0.4$. The jets used in this study are calibrated using the EM+JES scheme [36].

Tracks are associated to jets by the ghost-association procedure [37, 38]. This procedure assigns approximately zero momentum to all tracks, and then runs the anti-k_t algorithm on the clusters and these negligible momentum tracks. The anti-k_t algorithm then uniquely associates the tracks to the jets without changing the momentum of the jet.

The jet-vertex-tagger [39] (JVT) technique may be used to separate hard scatter jets from pile-up jets in the central region of the detector. This uses a multivariate combination of track-based variables to quantify the likelihood that a jet originates from the hard-scatter process. Values of JVT range between 0 (probably a pile-up jet) to 1 (probably a hard-scatter jet). Jets with no associated tracks are assigned a value JVT = −0.1. This technique compares favourably to the jet vertex fraction [40] (JVF) previously used, as JVT displays better pile-up jet rejection for a given hard-scatter jet efficiency [39].

Imposing a condition on the JVT brings with it a trade-off between eliminating pile-up jets and removing jets from the hard scatter. For the CST $E^{\text{miss}}_{\text{T}}$, no requirement is placed on the JVT as the calorimeter-based soft term includes the soft recoil from all interactions. For the TST $E^{\text{miss}}_{\text{T}}$, a jet-vertex-tagger requirement JVT > 0.64 is applied to jets. This maintains the balance of the jet term with the pile-up-robust track-based soft term. This JVT working point gives an efficiency of 92% in selecting hard-scatter jets. In the case of the TST $E^{\text{miss}}_{\text{T}}$, the tracks matched to jets which fail this requirement will enter the soft term (provided they are associated with the primary vertex). For this performance analysis, an additional condition was imposed, to combat a bias in the JVT selection for pile-up jets in the vicinity of a muon: jets are excluded if the overlap-removal with a muon would reduce the apparent jet p_{T} by more than 90%, providing the calorimeter-based p_{T} reduction is small.

Jets resulting from pile-up interactions are on the whole softer than those resulting from a hard scatter. A threshold in p_{T} is therefore applied to those jets entering the $E^{\text{miss}}_{\text{T}}$ jet term. Figure 2a shows the effect on

(a) $E_{\mathrm{T}}^{\mathrm{miss}}$ resolution vs N_{PV} (b) $E_{\mathrm{T}}^{\mathrm{miss}} \parallel p_{\mathrm{T}}^{Z}$
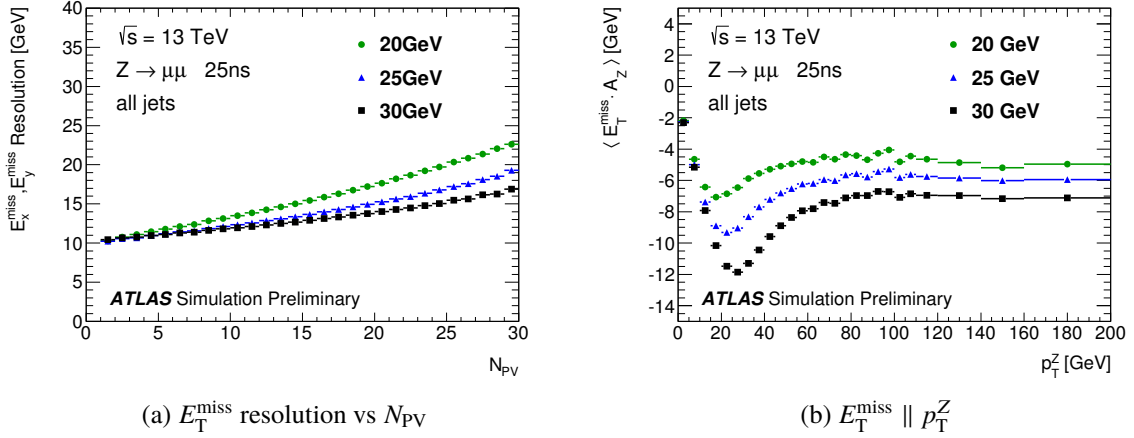
Figure 2: TST $E_{\mathrm{T}}^{\mathrm{miss}}$ performance shown in POWHEG+PYTHIA simulated $Z \to \mu\mu$ events for different values of the jet p_{T} threshold, as quantified by (a) the resolution as a function of the number of primary vertices and (b) the projection of $E_{\mathrm{T}}^{\mathrm{miss}}$ along the direction of the Z boson p_{T}. The resolution is defined as the root-mean-square (RMS) of the $E_{x(y)}^{\mathrm{miss}}$ distribution. E_x^{miss} and E_y^{miss} are found to have the same RMS, so the two distributions are combined.

the TST $E_{\mathrm{T}}^{\mathrm{miss}}$ resolution of the value of the threshold applied for events containing an arbitrary number of jets (specified as "all jets" in the figures in this note). Higher values of the threshold reduce the effect of pile-up on $E_{\mathrm{T}}^{\mathrm{miss}}$, and so improve the resolution of the reconstruction. However at high values of the jet p_{T} threshold, the $E_{\mathrm{T}}^{\mathrm{miss}}$ becomes biased against the direction of the Z boson, as hard-scatter jets are falsely removed. This can be seen in Fig. 2b, which shows the TST $E_{\mathrm{T}}^{\mathrm{miss}}$ projected along the direction of the Z transverse momentum. Raising the jet p_{T} above 20 GeV brings an improvement in resolution, but at the cost of a significant bias in $E_{\mathrm{T}}^{\mathrm{miss}}$ direction. For this reason, 20 GeV is set as the minimum calibrated p_{T} to select a jet.

5.2 Calorimeter soft term (CST)

The calorimeter soft term [1] (CST) is reconstructed from the energy deposits in calorimeter cells, grouped into topoclusters, which are not associated with reconstructed hard objects. Only energy contributions from calorimeter cells belonging to a topocluster are included in the CST. The energies recorded in this way are calibrated at the LCW scale [34, 41].

The $E_{\mathrm{T}}^{\mathrm{miss}}$ as calculated using a calorimeter soft term is known as "CST $E_{\mathrm{T}}^{\mathrm{miss}}$", and was the standard $E_{\mathrm{T}}^{\mathrm{miss}}$ definition used in most Run 1 analyses.

5.3 Track soft term (TST)

The track soft term (TST) is built from ID tracks satisfying the selection conditions described in Section 4.1 but not matched to any reconstructed object. Only those tracks associated with the hard scatter vertex are included. Tracks are excluded if they are within $\Delta R = 0.05$ of an electron or photon cluster, or within $\Delta R = 0.2$ of a hadronically-decaying tau-lepton. ID tracks from combined or segment-tagged muons are replaced by a combined fit to the ID and MS tracks. Tracks associated with jets using the ghost-association

technique [37, 38] are removed, as are tracks with momentum uncertainties larger than 40% or with no matching calorimeter deposit.

Since tracks may be accurately matched to a primary vertex, the TST is relatively insensitive to pile-up effects. It does not, however, include contributions from soft neutral particles and from forward regions ($|\eta| > 2.5$). The $E_{\mathrm{T}}^{\mathrm{miss}}$ as calculated using the track soft term is known as "TST $E_{\mathrm{T}}^{\mathrm{miss}}$".

5.4 Track $E_{\mathrm{T}}^{\mathrm{miss}}$

Track $E_{\mathrm{T}}^{\mathrm{miss}}$ takes advantage of the excellent vertex resolution of the ATLAS detector by using track information in the $E_{\mathrm{T}}^{\mathrm{miss}}$ hard terms. This gives a very pile-up-robust $E_{\mathrm{T}}^{\mathrm{miss}}$ estimation, but neglects the contribution of neutral particles, which do not form tracks in the ID. The η coverage of Track $E_{\mathrm{T}}^{\mathrm{miss}}$ is also limited to the tracking volume of $|\eta| < 2.5$, which is smaller than the calorimeter coverage extending to $|\eta| = 4.9$.

The Track $E_{\mathrm{T}}^{\mathrm{miss}}$ is reconstructed as the negative sum of the momenta of ID tracks satisfying the selection conditions described in Section 4.1. Due to interactions within the ID, the electron p_{T} is more precisely measured using the calorimeter than using the track momentum. Therefore, the p_{T} of an electron track is replaced by the calorimeter cluster measurement. For Track $E_{\mathrm{T}}^{\mathrm{miss}}$, the soft term is reconstructed from ID tracks satisfying the selection conditions of Section 4.1 but not matched to either electrons or muons.

6 Event selection

6.1 $Z \rightarrow \ell\ell$ event selection

The selection of $Z \rightarrow \ell\ell$ events requires there be exactly two selected leptons (defined as in Sections 4.2 and 4.3) with $p_{\mathrm{T}} > 25$ GeV. Electrons falling in the transition region between the barrel and end-cap electromagnetic calorimeters, $1.37 < |\eta| < 1.52$, are not considered. The leptons must be of the same flavour (electron or muon) and of opposite charge. The reconstructed invariant mass of the dilepton system, $m_{\ell\ell}$, is required to be consistent with the mass of the Z boson ($|m_{\ell\ell} - m_Z| < 25$ GeV).

6.2 $W \rightarrow \ell\nu$ event selection

Lepton candidates are selected based on criteria described in Sections 4.2 and 4.3. Events are required to contain exactly one good lepton. Selections on the $E_{\mathrm{T}}^{\mathrm{miss}}$ and reconstructed transverse mass are used to reduce the background from multijet events where one jet mimics the isolated lepton from the W boson. The $E_{\mathrm{T}}^{\mathrm{miss}}$, calculated as described in Section 5, is required to be greater than 25 GeV. The reconstructed transverse mass of the lepton and the $E_{\mathrm{T}}^{\mathrm{miss}}$ is defined as

$$m_{\mathrm{T}} = \sqrt{2p_{\mathrm{T}}^{\ell} E_{\mathrm{T}}^{\mathrm{miss}} (1 - \cos \Delta\phi)} \tag{5}$$

where p_{T}^{ℓ} is the transverse momentum of the lepton and $\Delta\phi$ is the azimuthal angle between the lepton momentum and $E_{\mathrm{T}}^{\mathrm{miss}}$. In order to maintain a consistent set of events when comparing $E_{\mathrm{T}}^{\mathrm{miss}}$ definitions, these two requirements are made always using the TST $E_{\mathrm{T}}^{\mathrm{miss}}$. The transverse mass is required to be greater than 40 GeV.
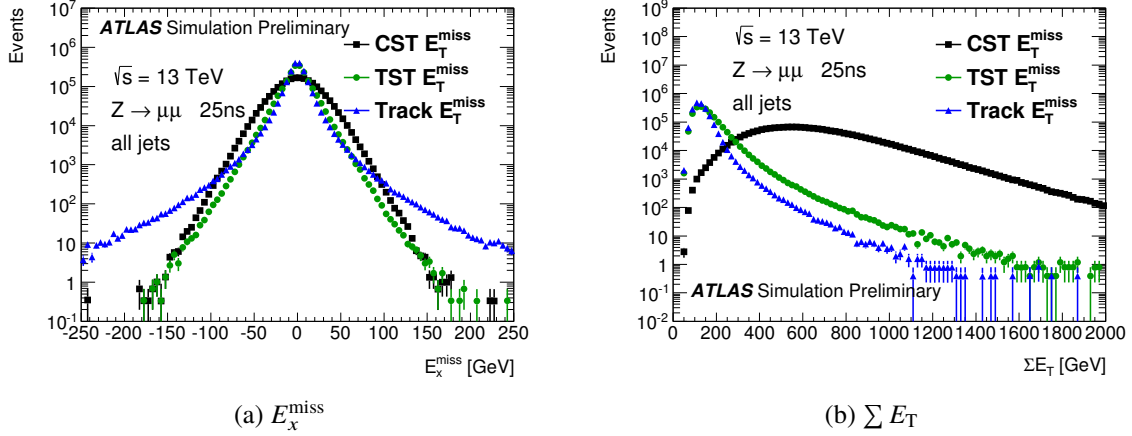
(a) E_x^{miss}

(b) $\sum E_{\mathrm{T}}$

Figure 3: Distributions of (a) the x component of the total $E_{\mathrm{T}}^{\mathrm{miss}}$, and (b) $\sum E_{\mathrm{T}}$. These are shown for the TST $E_{\mathrm{T}}^{\mathrm{miss}}$, CST $E_{\mathrm{T}}^{\mathrm{miss}}$ and Track $E_{\mathrm{T}}^{\mathrm{miss}}$ definitions, using POWHEG+PYTHIA $Z \rightarrow \mu\mu$ simulated events.

6.3 $t\bar{t}$ event selection

Only lepton plus jets $t\bar{t}$ events are considered, that is, requiring exactly one lepton (electron or muon) in the event. Lepton candidates are selected based on criteria described in Sections 4.2 and 4.3.

7 Performance of missing transverse momentum

7.1 $E_{\mathrm{T}}^{\mathrm{miss}}$ distributions

In this section, the behaviour of the reconstructed $E_{\mathrm{T}}^{\mathrm{miss}}$ is examined in Monte Carlo simulated events.

As mentioned, $Z \rightarrow \ell\ell$ events are the primary standard for evaluation of $E_{\mathrm{T}}^{\mathrm{miss}}$ performance owing to the absence of genuine missing momentum. A non-zero mean $E_{\mathrm{T}}^{\mathrm{miss}}$ is indicative of biases in $E_{\mathrm{T}}^{\mathrm{miss}}$, while the spread about the mean is a measure of the resolution of $E_{\mathrm{T}}^{\mathrm{miss}}$ reconstruction. $Z \rightarrow \ell\ell$ events are therefore a good choice for the study of imperfections in the $E_{\mathrm{T}}^{\mathrm{miss}}$ reconstruction process. All the distributions in this subsection are normalised to an integrated luminosity of 1 fb^{-1}.

Figure 3a compares the distributions of the missing transverse momentum components along the x axis as reconstructed using the three alternative definitions TST $E_{\mathrm{T}}^{\mathrm{miss}}$, CST $E_{\mathrm{T}}^{\mathrm{miss}}$ and Track $E_{\mathrm{T}}^{\mathrm{miss}}$. The TST $E_{\mathrm{T}}^{\mathrm{miss}}$ and CST $E_{\mathrm{T}}^{\mathrm{miss}}$ definitions show very similar tails, while the TST $E_{\mathrm{T}}^{\mathrm{miss}}$ has a narrower peak. For Track $E_{\mathrm{T}}^{\mathrm{miss}}$, the tails visible at high $|E_x^{\mathrm{miss}}|$ are mostly attributable to a lack of sensitivity to neutral particles in jets. There is also a contribution from the reduced η acceptance of the ID as compared to the calorimeter, which plays different roles depending on the event topology. Figure 3b shows the distribution of $\sum E_{\mathrm{T}}$, which is a measure of event activity defined in Eq. 4. The CST $E_{\mathrm{T}}^{\mathrm{miss}}$ shows greater event activity, owing largely to its lack of discrimination against pile-up by primary vertex. The difference between the TST $E_{\mathrm{T}}^{\mathrm{miss}}$ and Track $E_{\mathrm{T}}^{\mathrm{miss}}$ reveals the contribution of neutral particles, to which the calorimeter-based jet term is sensitive, but the track-based method is not. The performance of $E_{\mathrm{T}}^{\mathrm{miss}}$ reconstruction is similar between $Z \rightarrow \mu\mu$ and $Z \rightarrow ee$ events, and so only $Z \rightarrow \mu\mu$ samples are shown in this and subsequent figures.
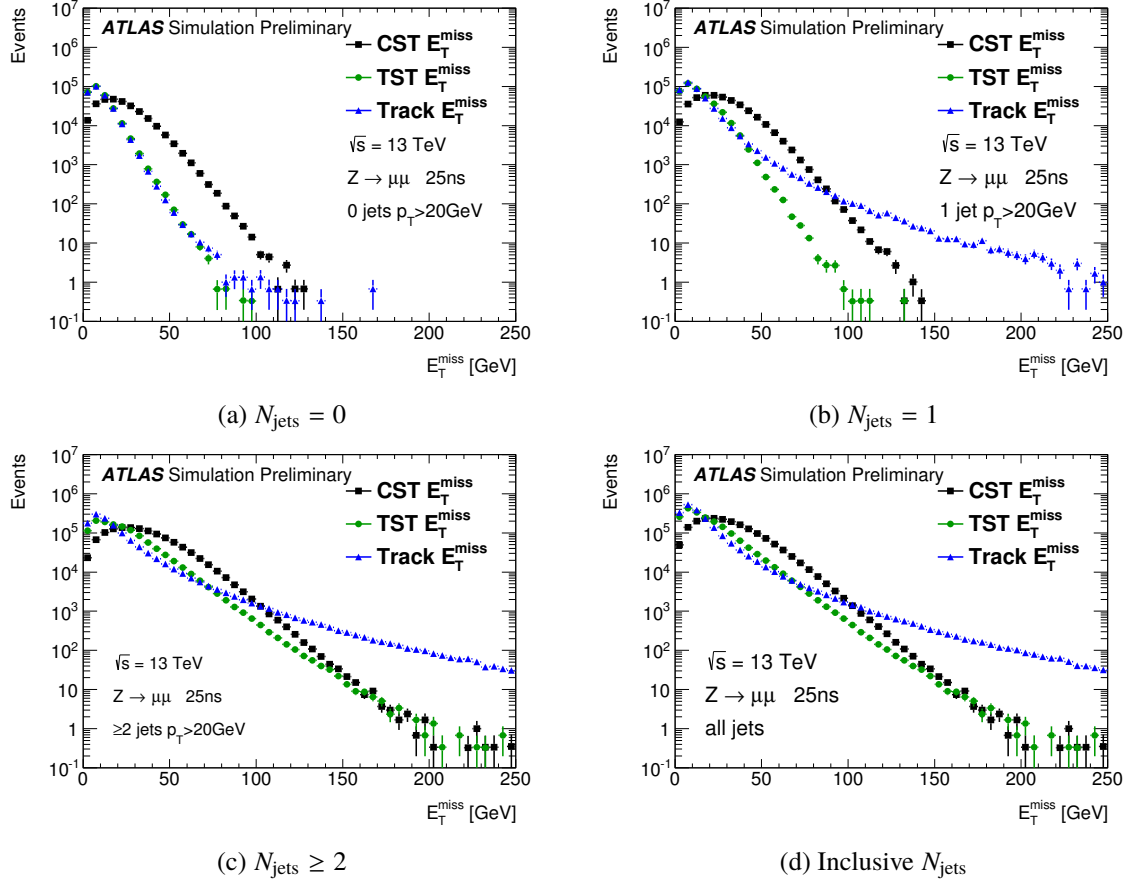
(a) $N_{\text{jets}} = 0$

(b) $N_{\text{jets}} = 1$

(c) $N_{\text{jets}} \geq 2$

(d) Inclusive N_{jets}

Figure 4: Distributions of the total TST E_T^{miss}, CST E_T^{miss} and Track E_T^{miss}, shown for POWHEG+PYTHIA $Z \to \mu\mu$ simulated events. The distributions are separated based on the number of calibrated jets with $p_T > 20\,\text{GeV}$. The four figures separately show events with 0, 1, and 2 or more jets. (d) shows events for all N_{jets}.

Figure 4 compares the distributions of total missing transverse momentum as reconstructed using TST E_T^{miss}, CST E_T^{miss}, and Track E_T^{miss}. Distributions for events containing 0, 1, and 2 or more reconstructed jets are shown separately in order to illustrate the effect on the E_T^{miss} distribution. To allow comparison between definitions, the jet multiplicity (N_{jets}) is defined on jets without conditions on JVT.

For events with no hard jets, TST E_T^{miss} and Track E_T^{miss} are expected to be similar, since their soft terms are defined by the same procedure. For the $Z \to \mu\mu$ topology prompt tau-leptons and photons are not expected. The small difference for $E_T^{\text{miss}} \gtrsim 50\,\text{GeV}$ in Fig. 4a is then primarily attributable to jets mistakenly reconstructed as hadronically-decaying tau-leptons or photons, which are included in the TST E_T^{miss} but escape the Track E_T^{miss}. Figure 4a shows that the contribution of fake hadronically-decaying tau-leptons and photons has little impact on the reconstruction of E_T^{miss}. For event with few hard jets, the distribution of TST E_T^{miss} is noticeably softer than that of CST E_T^{miss}. This difference comes mostly from the robustness of the TST E_T^{miss} under pile-up, and is diminished for higher multiplicities of hard jets, where the identical jet terms gain prominence.

The soft term distributions are shown separately in Fig. 5. In the case $N_{\text{jets}} = 0$, the TST and Track E_T^{miss} soft term differ only in the contribution of hadronically-decaying tau-lepton candidates (or jets falsely identified as such). For TST E_T^{miss}, the tracks associated with this tau-lepton candidate are matched to
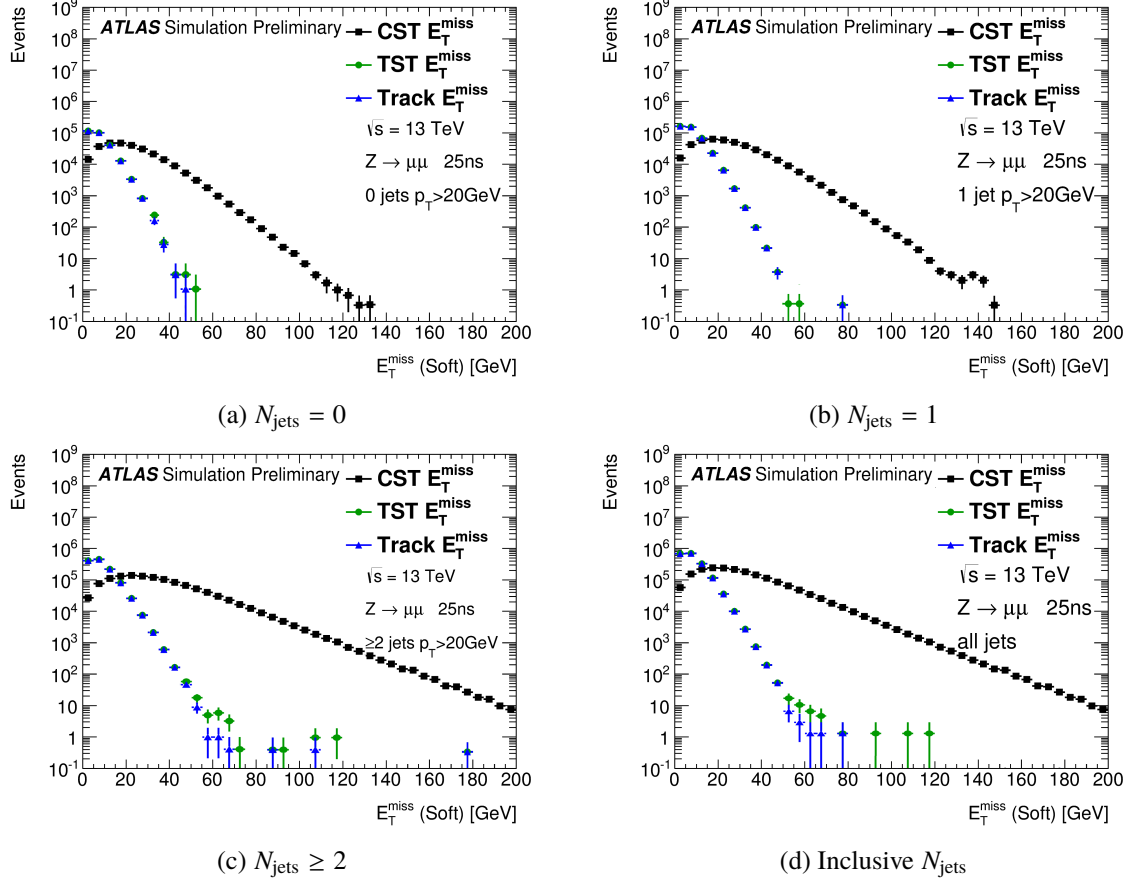
(a) $N_{\text{jets}} = 0$

(b) $N_{\text{jets}} = 1$

(c) $N_{\text{jets}} \geq 2$

(d) Inclusive N_{jets}

Figure 5: Distributions of the $E_{\text{T}}^{\text{miss}}$ soft term as reconstructed by the TST, CST, and Track $E_{\text{T}}^{\text{miss}}$ methods, shown for POWHEG+PYTHIA $Z \to \mu\mu$ Monte Carlo simulated events. The distributions are separated based on the number of calibrated jets with $p_{\text{T}} > 20\,\text{GeV}$. The four figures separately show events with 0, 1, and 2 or more jets. (d) shows events for all N_{jets}.

a calorimeter cluster, and enter $E_{\text{T}}^{\text{miss}}$ in the tau term. For Track $E_{\text{T}}^{\text{miss}}$, the tracks are incorporated into the soft term. For $N_{\text{jets}} > 0$, TST and Track $E_{\text{T}}^{\text{miss}}$ additionally differ in that the Track $E_{\text{T}}^{\text{miss}}$ includes the contribution of tracks inside high-p_{T} jets.

7.2 $E_{\text{T}}^{\text{miss}}$ response

In $Z \to \mu\mu$ events, the axis defined by the p_{T} of the Z boson is useful to identify biases in the detector response. The unit vector along this axis is defined as

$$A_Z = \frac{\mathbf{p_T}^{\ell^+} + \mathbf{p_T}^{\ell^-}}{|\mathbf{p_T}^{\ell^+} + \mathbf{p_T}^{\ell^-}|}, \tag{6}$$

where $\mathbf{p_T}^{\ell^+}$ and $\mathbf{p_T}^{\ell^-}$ are the transverse momenta of the leptons from the Z boson decay.

The mean value of the $\mathbf{E_T}^{\text{miss}}$ projected onto A_Z ($\langle \mathbf{E_T}^{\text{miss}} \cdot A_Z \rangle$) is a measure of the $E_{\text{T}}^{\text{miss}}$ scale, sensitive to the balance between the leptons and the soft hadronic recoil. For perfect balance of the leptons against

12

the soft hadronic recoil, the projection of $\mathbf{E}_T^{miss}$ onto A_Z would be zero. Figures 6a and 6b show the projection of $\mathbf{E}_T^{miss}$ onto A_Z for $Z \rightarrow \mu\mu$ events with zero and any number of jets respectively. The projection is negative for all E_T^{miss} definitions, which for zero-jet events indicates an underestimation of the soft recoil. In the zero-jet case, there is reasonable agreement between the three E_T^{miss} definitions. The track-based methods show a slightly greater underestimation of the soft recoil, owing to their insensitivity to soft neutral particles. If events with $N_{jet} > 0$ are included, Track E_T^{miss} displays an increasing projection along the axis of the Z boson. This is attributed to the loss of neutral particles from high-p_T jets recoiling against the Z boson. The difference between the CST E_T^{miss} and the TST E_T^{miss} for $p_T^Z > 40\,\text{GeV}$ indicates a slightly greater imbalance for the CST E_T^{miss}. An similar effect is expected from the imperfect treatment of energy loss by the muons in the calorimeter-based soft term [1].

The presence of a neutrino in the $W \rightarrow \ell\nu$ final state means that these events come with "genuine" E_T^{miss}. These events are therefore useful to evaluate the E_T^{miss} scale. The figures shown in this section are for the muon final state $W \rightarrow \mu\nu$. No significant differences are observed between the distributions for $W \rightarrow \mu\nu$ and for $W \rightarrow e\nu$.

The "linearity" is defined as

$$\text{linearity} = \left\langle \frac{E_T^{miss} - E_T^{miss,True}}{E_T^{miss,True}} \right\rangle \tag{7}$$

and measures the consistency between the true and reconstructed E_T^{miss}. If E_T^{miss} were reconstructed at the correct scale, the linearity would be zero. Figures 6c, 6d and 7 show the linearity against $E_T^{miss,True}$ for $W \rightarrow \mu\nu$ and $t\bar{t}$ simulated events. Since E_T^{miss} is by definition positive and has a finite resolution, a positive bias in the linearity at low $E_T^{miss,True}$ is expected[3]. At higher $E_T^{miss,True}$, CST E_T^{miss} and TST E_T^{miss} reconstruct the correct scale to better than 5% accuracy. Track E_T^{miss} significantly underestimates the E_T^{miss} scale, as it omits the contribution of neutral particles within jets.

7.3 E_T^{miss} resolution

The performance of E_T^{miss} reconstruction may be quantified by the observed width of the E_T^{miss} distribution. In some previous studies [1], this was expressed as the width of a Gaussian fit to $E_{x,y}^{miss}$. Here, the root-mean-square (RMS) of the distribution is used, in order to better accommodate the non-Gaussian tails observed in track-based E_T^{miss} methods. The resulting comparison between TST E_T^{miss}, CST E_T^{miss} and Track E_T^{miss}, as a function of the scalar sum of transverse energy in the event using the CST object definitions and soft term (CST $\sum E_T$) is shown in Fig. 8. In both $Z \rightarrow \mu\mu$ and $W \rightarrow \mu\nu$ events, the CST has a steadily increasing width with increasing event activity. The track-based methods are rather less sensitive to this. This change is partly attributable to increasing jet resolution, hence its influence on the TST E_T^{miss} but not on Track E_T^{miss}. At low $\sum E_T$ and in events with no hard jets, TST E_T^{miss} is dominated by the soft hadronic recoil, and so is very similar to Track E_T^{miss}. As the event activity increases, TST E_T^{miss} converges on CST E_T^{miss}, as the contribution of jets comes to dominate.

The resolution in simulated $t\bar{t}$ events is shown in Fig. 9. This topology demonstrates the effect of a high jet multiplicity: typical events have $N_{jets} \geq 4$, as compared to 1–2 jets for $W \rightarrow \ell\nu$ events. Here, the behaviour of CST E_T^{miss} is very similar to its behaviour for $Z \rightarrow \mu\mu$ and $W \rightarrow \mu\nu$ events, its resolution being little degraded by the increased event activity. TST E_T^{miss} and CST E_T^{miss} resolutions are very similar,

---

[3] In addition, the selection of $W \rightarrow \mu\nu$ events requires TST $E_T^{miss} > 25\,\text{GeV}$

(a) $\langle \mathbf{E}_T^{miss} \cdot A_Z \rangle$, $N_{jets} = 0$

(b) $\langle \mathbf{E}_T^{miss} \cdot A_Z \rangle$, inclusive N_{jets}

(c) E_T^{miss} linearity, $N_{jets} = 0$

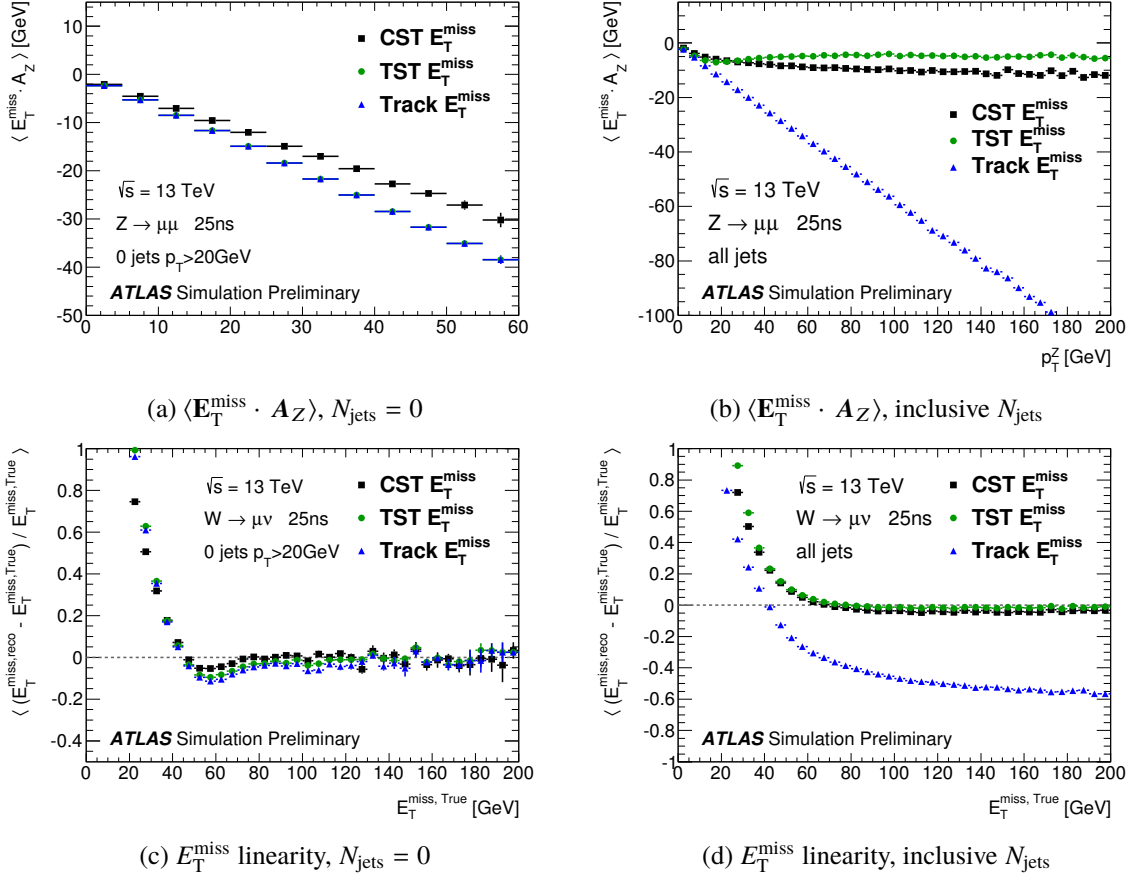(d) E_T^{miss} linearity, inclusive N_{jets}

Figure 6: Comparison for TST E_T^{miss}, CST E_T^{miss} and Track E_T^{miss}, of (a,b): the mean projection of E_T^{miss} along the direction of the Z in POWHEG+PYTHIA $Z \rightarrow \mu\mu$ events; and (c,d): E_T^{miss} linearity as a function of $E_T^{miss,True}$ in POWHEG+PYTHIA $W \rightarrow \mu\nu$ events. For perfect scale agreement between reconstructed and true E_T^{miss}, a zero value of linearity would be expected.

as in this topology the resolution is dominated by the jet term, which they have in common. The resolution of the Track E_T^{miss} suffers, owing to the increased jet multiplicity, from which neutral particles are lost.

As a more direct measure of the performance of E_T^{miss} under varying pile-up conditions, the resolution in E_x^{miss} and E_y^{miss} is shown as a function of the number of primary vertices in the event, N_{PV}. The resulting comparison is shown for $Z \rightarrow \mu\mu$ events in Fig. 10. $W \rightarrow \mu\nu$ events exhibit very similar behaviour. The resolution of CST E_T^{miss} increases with an increasing number of primary vertices. This is to be expected, as the additional interactions deposit energy in the calorimeter which the calorimeter-based method cannot distinguish from the deposits of the hard-scatter process. The resolution of Track E_T^{miss} has very little dependence on the number of primary vertices, since tracks may be effectively associated to the hard-scatter vertex. When hard jets are present in events with low N_{PV}, the track-based method displays a larger resolution than calorimeter-based methods, owing to its neglect of neutral particles. The TST E_T^{miss} displays a hybrid behaviour, combining the small resolution at low N_{PV} with the flat profile of the track-based method in events with no hard jets.
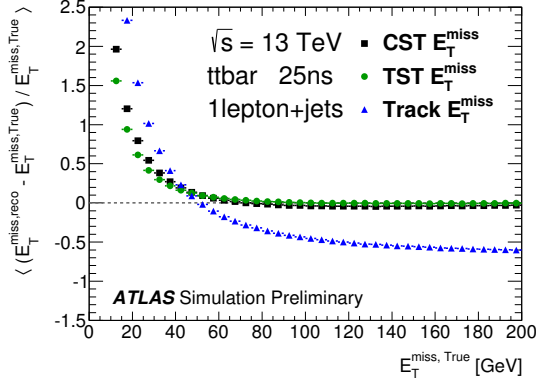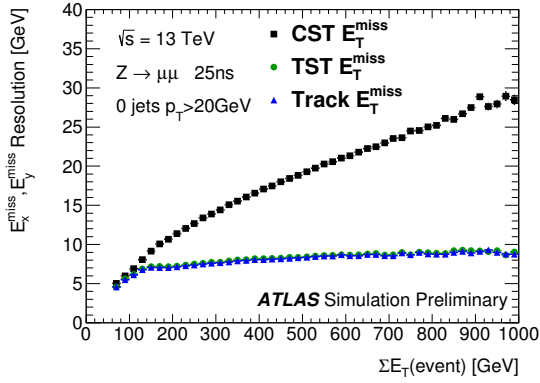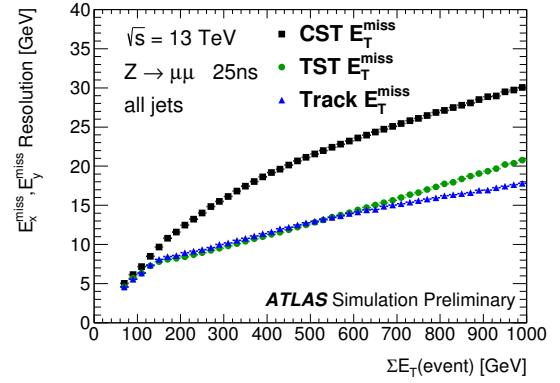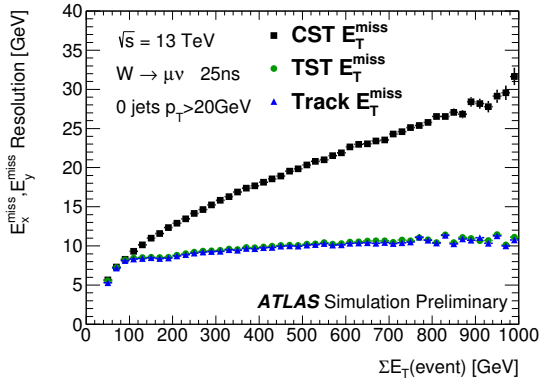
Figure 7: Comparison of the response of TST E_T^{miss}, CST E_T^{miss} and Track E_T^{miss}, as quantified by the E_T^{miss} linearity as a function of $E_T^{miss,True}$ in $t\bar{t}$ events. For perfect scale agreement between reconstructed and true E_T^{miss}, a zero value of linearity would be expected.
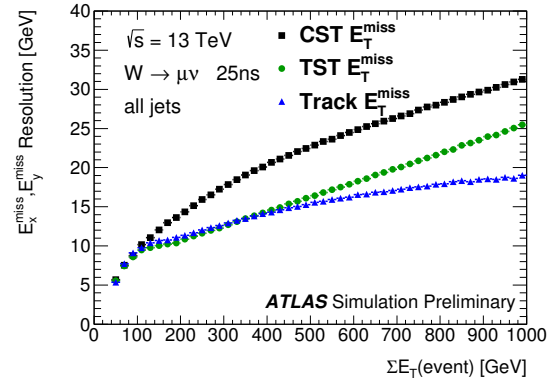

(a) $Z \to \mu\mu$: E_T^{miss} resolution $N_{jets} = 0$

(b) $Z \to \mu\mu$: E_T^{miss} resolution inclusive N_{jets}

(c) $W \to \mu\nu$: E_T^{miss} resolution $N_{jets} = 0$

(d) $W \to \mu\nu$: E_T^{miss} resolution inclusive N_{jets}

Figure 8: Comparison of the performance of E_T^{miss} built from TST and CST, and the Track E_T^{miss}, as quantified by the resolution (RMS of E_x^{miss}, E_y^{miss}), as a function of the CST $\sum E_T$. Powheg+Pythia $Z \to \mu\mu$ and $W \to \mu\nu$ samples are shown.
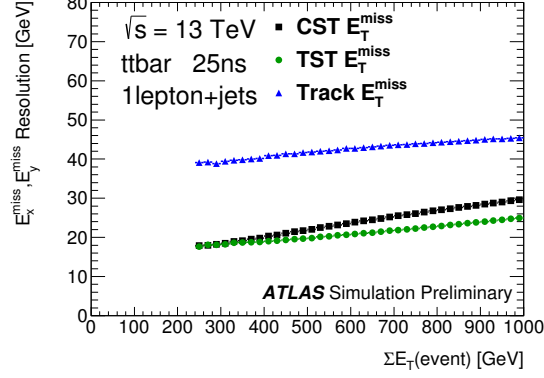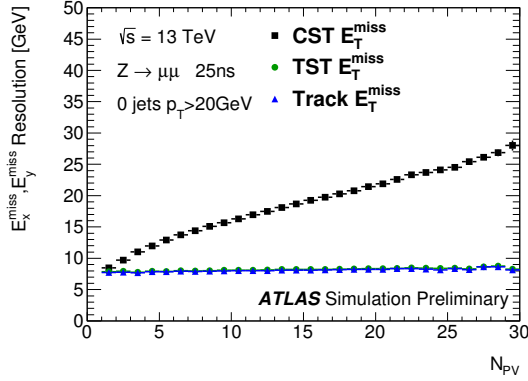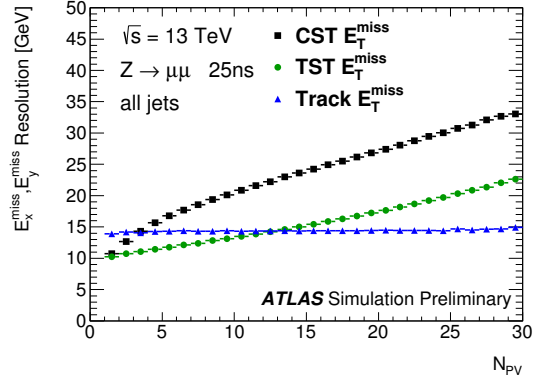
15

Figure 9: Comparison of the performance of TST E_T^{miss}, CST E_T^{miss} and Track E_T^{miss}, as quantified by the resolution (RMS of E_x^{miss}, E_y^{miss}) as a function of CST $\sum E_T$ in $t\bar{t}$ events.

(a) $Z \to \mu\mu$: E_T^{miss} resolution $N_{jets} = 0$

(b) $Z \to \mu\mu$: E_T^{miss} resolution inclusive N_{jets}

Figure 10: Comparison of the performance of E_T^{miss} built from TST and CST, and the Track E_T^{miss}, under varying pile-up conditions. The resolution (RMS of E_x^{miss}, E_y^{miss}) is shown as a function of N_{PV} for POWHEG+PYTHIA $Z \to \mu\mu$ events.

8 Systematic uncertainties

The systematic uncertainties on $E_{\mathrm{T}}^{\mathrm{miss}}$ quantify the level of agreement between data and Monte Carlo simulation. These are handled on a term-by-term basis, according to the components given in Eq. 1. The uncertainties provided for the electrons, muons, jets, hadronically decaying tau-leptons, and photons are propagated into their respective $E_{\mathrm{T}}^{\mathrm{miss}}$ terms. This section therefore focuses on the derivation of systematic uncertainties for the $E_{\mathrm{T}}^{\mathrm{miss}}$ soft term.

As explained in Section 1, TST $E_{\mathrm{T}}^{\mathrm{miss}}$ is the primary $E_{\mathrm{T}}^{\mathrm{miss}}$ definition for Run 2. The systematic uncertainties for the track-based soft term are discussed in Section 8.1. Studies of the systematic uncertainties in the CST (the primary $E_{\mathrm{T}}^{\mathrm{miss}}$ definition in Run 1) will not be presented here.

In previous studies, data-driven techniques were used to evaluate the systematic uncertainties. The purpose of the current study is to provide an estimate of the systematic uncertainty for analyses operating early in Run 2. Modified techniques exploiting the differences between Monte Carlo generators are therefore employed.

In Run 1, it was found that the difference between data and Monte Carlo simulation was smaller than the range given by different MC event generators. This estimation of Run 2 systematic uncertainties therefore follows a method of comparing several different MC simulations of 13 TeV running conditions. One generator is chosen as the "nominal" sample, and the spread of alternative generators about this is taken to cover the difference between data and simulation. POWHEG+PYTHIA8 was chosen as the nominal generator, on account of the favourable number of simulated events available and agreement with data in Run 1. In addition to this modelling uncertainty, there are changes in the detector and running conditions whose effects have some associated uncertainty. The variation owing to these is found to be small compared to the modelling uncertainty, but non-negligible. The derived systematic uncertainty is therefore a combination of all these contributions. For details of all the generators used, see Section 3 and Ref. [42].

In quantifying the systematic uncertainty, it is useful to define $\mathbf{p}_{\mathrm{T}}^{\mathrm{hard}}$, the vector sum of the transverse momenta of the hard objects in the event:

$$\mathbf{p}_{\mathrm{T}}^{\mathrm{hard}} = \sum \mathbf{p}_{\mathrm{T}}^{\mathrm{e}} + \sum \mathbf{p}_{\mathrm{T}}^{\gamma} + \sum \mathbf{p}_{\mathrm{T}}^{\tau} + \sum \mathbf{p}_{\mathrm{T}}^{\mathrm{jet}} + \sum \mathbf{p}_{\mathrm{T}}^{\mu} + \sum \mathbf{p}_{\mathrm{T}}^{\nu}. \tag{8}$$

The uncertainties in the missing transverse momentum vary depending on the amount of high-p_{T} activity in the event. A measure of this is given by the magnitude of $\mathbf{p}_{\mathrm{T}}^{\mathrm{hard}}$, denoted by $p_{\mathrm{T}}^{\mathrm{hard}}$.

To have zero total momentum in the transverse plane, the $E_{\mathrm{T}}^{\mathrm{miss}}$ soft term should balance $\mathbf{p}_{\mathrm{T}}^{\mathrm{hard}}$. Differences from this show problems in the calibration of objects contributing to $E_{\mathrm{T}}^{\mathrm{miss}}$. The axis defined by $\mathbf{p}_{\mathrm{T}}^{\mathrm{hard}}$ is useful to isolate scale offsets (primarily longitudinal to $\mathbf{p}_{\mathrm{T}}^{\mathrm{hard}}$) from resolution (components both longitudinal and transverse to $\mathbf{p}_{\mathrm{T}}^{\mathrm{hard}}$).

The soft terms for both the TST $E_{\mathrm{T}}^{\mathrm{miss}}$ and Track $E_{\mathrm{T}}^{\mathrm{miss}}$ definitions are constructed from tracks not associated with hard objects. The two differ in that tracks inside high-p_{T} jets are used in the Track $E_{\mathrm{T}}^{\mathrm{miss}}$, but not in the TST. These additional tracks considered for the Track $E_{\mathrm{T}}^{\mathrm{miss}}$ give an extra contribution to the systematic uncertainty, which will be discussed in Section 8.2.

8.1 Track Soft Term systematic uncertainties

This section describes the systematic uncertainty assigned to the track-based soft term as used in both the TST E_T^{miss} and Track E_T^{miss} definitions. These uncertainties quantify the resolution and scale of the soft term measurement by using the balance between hard and soft contributions in $Z \to \mu\mu$ events.

The soft term for each of the different generated samples is decomposed into components longitudinal and transverse to $\mathbf{p}_T^{hard}$. The difference between these distributions for different generators is taken to reflect the uncertainty in the E_T^{miss} reconstruction. With this in mind, the distributions are convolved with a Gaussian smearing function, whose parameters are fixed by a fit to a nominal sample. The fit is done in bins of p_T^{hard}, with the bin width determined by the number of simulated events available. The samples are also binned based on the number of hard jets N_{jets} in the event. The fitted width of the Gaussian reflects the uncertainty in the resolution of the measurement, while the mean reflects the uncertainty in the scale.

Systematic uncertainties are assigned to the resolution longitudinal and transverse to $\mathbf{p}_T^{hard}$. The soft term scale longitudinal to $\mathbf{p}_T^{hard}$ is sensitive to the modelling of the hadronic recoil, and so a systematic uncertainty is also applied to this. There are then three components of a "generator systematic uncertainty", defined so as to cover the variations between the three generators examined.

In addition to the difference of event generators described above, systematic uncertainties are assigned to other aspects of Run 2 conditions. The effect on the E_T^{miss} reconstruction of an alternative azimuthal detector material distribution was investigated, using an alternative Powheg+Pythia sample as described in Section 3. The distributions of the E_T^{miss} soft term projections, binned in p_T^{hard} and N_{jets} as above, are compared between the nominal sample and the varied sample. The significance of the variation, as compared with expected statistical fluctuations, is assessed by means of a Kolmogorov-Smirnov test. An additional systematic uncertainty is assigned if there is a 5% or smaller probability that the difference in distributions is purely statistical variation. For the modification to detector geometry, the effect on the longitudinal scale is found to be small compared to the difference between generators. The change in the resolution (both longitudinal and transverse to $\mathbf{p}_T^{hard}$) is significant, however, and so an additional systematic uncertainty is ascribed to this variation.

The first period of LHC Run 2 data-taking will be using a proton bunch spacing of 50 ns. Whilst the standard Monte Carlo samples used a bunch spacing of 25 ns, an alternative sample was simulated using 50 ns. The same procedure is applied to this, in order to assess whether this variation has a significant impact on the uncertainty in soft term reconstruction. There are changes in the scale and in the longitudinal and transverse resolutions, and so an additional systematic uncertainty is assigned to each.

Some ATLAS analyses will make use of a fast detector simulation, ATLFAST 2 [23], as opposed to the full Geant4-based model. The effect on the derived systematic uncertainties of this alternative simulation was studied. There is no statistically significant difference in the E_T^{miss} soft term distribution in the component transverse to $\mathbf{p}_T^{hard}$. For the longitudinal scale and resolution, an additional systematic uncertainty is assigned.

These additional uncertainties are combined with the difference of generators under the assumption that these variations are independent, and summing their contribution in quadrature. This gives the final systematic uncertainties for the track-based soft term. By way of example, for p_T^{hard} in the range 20 – 40 GeV the systematic uncertainty derived for the scale is set at 0.9 GeV, of which 0.8 GeV is owing to the difference of generators and 0.4 GeV to the additional systematic uncertainty for the comparison of 25 ns and 50 ns bunch spacings. The variation in azimuthal material distribution has no impact on this
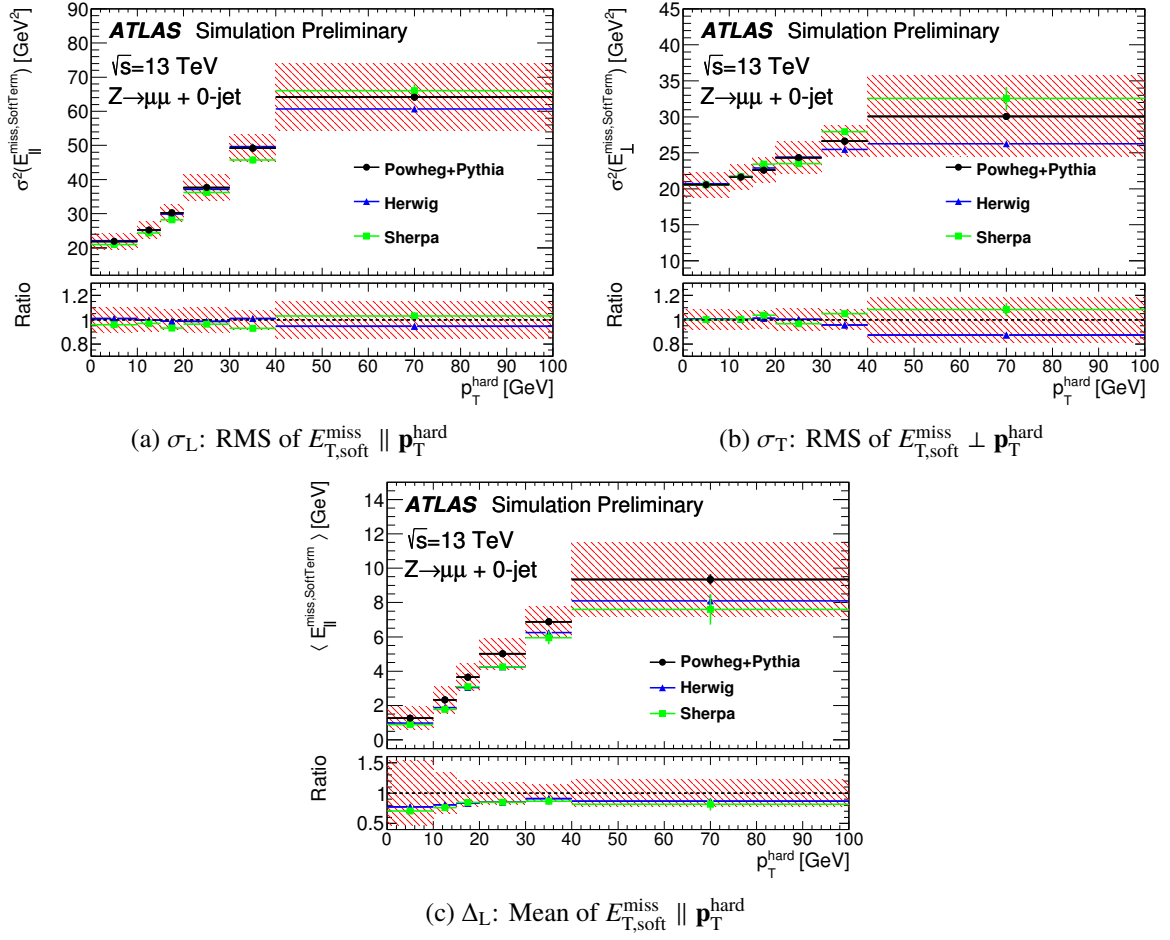
(a) σ_{L}: RMS of $E_{\mathrm{T,soft}}^{\mathrm{miss}} \parallel \mathbf{p}_{\mathrm{T}}^{\mathrm{hard}}$

(b) σ_{T}: RMS of $E_{\mathrm{T,soft}}^{\mathrm{miss}} \perp \mathbf{p}_{\mathrm{T}}^{\mathrm{hard}}$

(c) Δ_{L}: Mean of $E_{\mathrm{T,soft}}^{\mathrm{miss}} \parallel \mathbf{p}_{\mathrm{T}}^{\mathrm{hard}}$

Figure 11: RMS and mean of the $E_{\mathrm{T}}^{\mathrm{miss}}$ soft term projected into components longitudinal and transverse to $\mathbf{p}_{\mathrm{T}}^{\mathrm{hard}}$ in $Z \rightarrow \mu\mu$ 0-jet events. Points are shown for Powheg+Pythia8 (nominal), Herwig and Sherpa generators. The shaded band shows the effect of the TST systematic uncertainties with contributions from the difference of generators, the change in detector geometry and the variation in bunch spacing.

component. If fast simulation is used, a contribution of $0.2\,\mathrm{GeV}$ is added to cover for the difference in modelling between ATLFAST 2 and the full simulation.

The effect of the systematic uncertainties derived is illustrated in Fig. 11. Figures 11a and 11b show the root-mean-square widths of the soft term distributions, projected onto components longitudinal and transverse to $\mathbf{p}_{\mathrm{T}}^{\mathrm{hard}}$. Figure 11c shows the mean of the soft term longitudinal component. In each, points are shown for each of the generators employed. The combined effect of the three TST systematic uncertainty components on the total $E_{\mathrm{T}}^{\mathrm{miss}}$ distribution is illustrated in Fig. 12. The resolution smearing of the soft term results in a variation of roughly 2% that is constant with $E_{\mathrm{T}}^{\mathrm{miss}}$. The increasing spread at high $E_{\mathrm{T}}^{\mathrm{miss}}$ is owing to the downwards scale variation in the soft term, giving an upwards migration in $E_{\mathrm{T}}^{\mathrm{miss}}$ (since $E_{\mathrm{T}}^{\mathrm{miss}}$ is defined as a negative sum). The rapid fall of the distribution means the upwards scale variation has less effect, except in the lowest $E_{\mathrm{T}}^{\mathrm{miss}}$ bin.
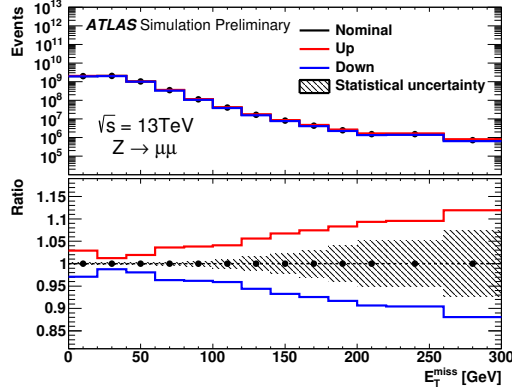
Figure 12: Total TST E_T^{miss}, and the variations on this resulting from the combined TST systematic uncertainties. POWHEG+PYTHIA8 $Z \to \mu\mu$ events are shown. The hatched band shows the statistical uncertainty in the ratio.

8.2 Track E_T^{miss} systematic uncertainties

Track E_T^{miss} is the sum of individual electrons, muons and the remaining tracks. For consistency with the TST E_T^{miss} soft term, the remaining tracks in the Track E_T^{miss} are divided into tracks associated to calorimeter jets (by the ghost-association procedure described in Section 5) satisfying the JVT requirement, and the non-associated tracks which constitute the soft term.

The total systematic uncertainty is then evaluated as follows:

- For the electron and muon terms, systematic uncertainties are propagated from those associated with the reconstructed objects.

- For the track soft term, the systematic uncertainties are similar to those derived for TST E_T^{miss} in Section 8.1, as these are built in the same way from tracks not associated with hard objects.

- For the tracks associated to calorimeter jets, uncertainties arise from several effects on the associated tracks and must be estimated independently.

This procedure allows a factorisation of the uncertainty into effects owing to the soft term (which is shared with the TST) and the effects owing to tracks within jets, such as the modelling of jet hadronisation. Measurements of the properties of tracks in jets were performed during Run 1 [43]; the systematic uncertainty described here follows this method. The ratio R is defined for each jet as

$$R = \frac{\sum p_T^{trk}}{p_T^{jet}}, \tag{9}$$

where the numerator is a scalar sum over the momenta of all tracks associated to the jet and passing tracking quality selections. p_T^{jet} is the p_T of the jet as measured by the calorimeter.

The following sources of systematic uncertainties are considered and their individual contributions to the variation of the R ratio extracted for selected jets:

- Effect of Monte Carlo generator modelling and tunes on tracks associated to jets.

- Effects of the detector material description on track reconstruction efficiency and track p_T resolution.
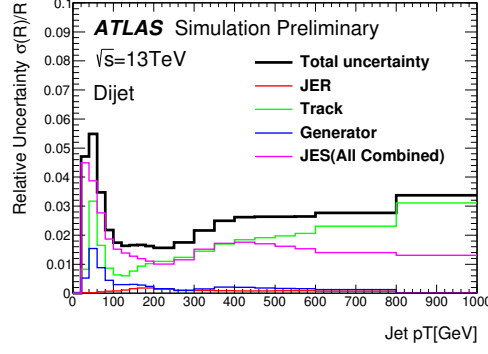
- Jet energy scale (JES) and jet energy resolution.

20

Figure 13: Contributions to the relative uncertainty in R, the ratio of the p_T of tracks within a jet to the reconstructed jet p_T. This distribution is for jet $|\eta|$ in the range 0–0.5.
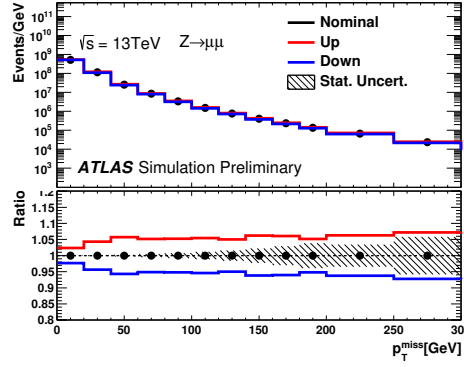

Figure 14: Total Track E_T^{miss} and the systematic variations on this resulting from the combination of the TST systematic uncertainty and the additional contribution for tracks inside jets. $Z \to \mu\mu$ events are shown. The hatched band shows the statistical uncertainty in the ratio.

The effect of the Monte Carlo generator is evaluated by comparing HERWIG++ to the nominal POWHEG. The resulting variations in R from all sources are combined and binned by jet p_T and $|\eta|$. Fig. 13 shows the contribution of each of these effects to the relative uncertainty in R for $|\eta|$ in the range $0-0.5$.

The total variations of R for each jet are propagated to the Track E_T^{miss} component associated to jets. The total systematic uncertainty is defined as the quadrature sum of the deviations with respect to the nominal value. Combining these uncertainties with those associated with Track Soft Term, as derived in Section 8.1, gives the total systematic uncertainty in the Track E_T^{miss}, as shown in Fig. 14.

9 Conclusions

The extensive solid angle coverage of the ATLAS detector allows the estimation of the total transverse momentum of particles not interacting with the detector, E_T^{miss}. Several different algorithms have been developed for the estimation of E_T^{miss}. In this study, the performance of these E_T^{miss} reconstruction algorithms is predicted using simulations of the ATLAS detector under Run 2 operating conditions.

Track-based methods, such as Track $E_{\mathrm{T}}^{\mathrm{miss}}$, offer improved stability under the conditions of increased pile-up expected in Run 2. The ID however has a limited coverage in η, and is insensitive to neutral particles. An alternative approach, CST $E_{\mathrm{T}}^{\mathrm{miss}}$, uses calorimeter measurements of both hard and soft objects. Calorimeter-based methods effectively gather information on high-p_{T} neutral particles, but suffer a degradation of performance owing to pile-up. By combining information from both the tracker and the calorimeter, it is possible to construct measures of the missing transverse momentum which effectively isolate the hard-scattering process, even under conditions of high pile-up.

The estimation of $E_{\mathrm{T}}^{\mathrm{miss}}$ comes with associated systematic uncertainties both in scale and resolution. The parametrisation of these is explained, and recommendations for the systematic uncertainties presented for both the TST $E_{\mathrm{T}}^{\mathrm{miss}}$ and the purely track-based Track $E_{\mathrm{T}}^{\mathrm{miss}}$.

References

[1] ATLAS Collaboration, *Performance of missing transverse momentum reconstruction in proton–proton collisions at $\sqrt{s}$ = 7 TeV with ATLAS*, Eur. Phys. J. C **72** (2012) 1844, arXiv: 1108.5602 [hep-ex].

[2] ATLAS Collaboration, *Performance of Missing Transverse Momentum Reconstruction in ATLAS with 2011 Proton–Proton Collisions at $\sqrt{s}$ = 7 TeV*, ATLAS-CONF-2012-101, 2012, URL: http://cdsweb.cern.ch/record/1463915.

[3] ATLAS Collaboration, *Performance of Missing Transverse Momentum Reconstruction in ATLAS studied in Proton–Proton Collisions recorded in 2012 at $\sqrt{s}$ = 8 TeV*, ATLAS-CONF-2013-082, 2013, URL: http://cdsweb.cern.ch/record/1570993.

[4] ATLAS Collaboration, *Pile-up Correction in Missing Transverse Momentum Reconstruction in the ATLAS Experiment in Proton–Proton Collisions at $\sqrt{s}$ = 8 TeV*, ATLAS-CONF-2014-019, 2014, URL: http://cdsweb.cern.ch/record/1702055.

[5] ATLAS Collaboration, *The ATLAS Simulation Infrastructure*, Eur. Phys. J. C **70** (2010) 823–874. 53 p, URL: https://cds.cern.ch/record/1267853.

[6] ATLAS Collaboration, *The ATLAS Experiment at the CERN Large Hadron Collider*, JINST **3** (2008) S08003.

[7] M. Capeans et al., *ATLAS Insertable B-Layer Technical Design Report*, Geneva, 2010, URL: https://cds.cern.ch/record/1291633.

[8] S. Artz et al., *Upgrade of the ATLAS Central Trigger for LHC Run-2*, JINST **10**.02 (2015) C02030.

[9] P. Nason, *A new method for combining NLO QCD with shower Monte Carlo algorithms*, JHEP **0411** (2004) 040, arXiv: hep-ph/0409146 [hep-ph].

[10] T. Sjostrand, S. Mrenna and P. Z. Skands, *A Brief Introduction to PYTHIA 8.1*, Comput.Phys.Commun. **178** (2008) 852–867, arXiv: 0710.3820 [hep-ph].

[11] H.-L. Lai et al., *New parton distributions for collider physics*, Phys. Rev. **D 82** (2010) 074024.

[12] ATLAS Collaboration, *Example ATLAS tunes of PYTHIA8, PYTHIA6 and POWHEG to an observable sensitive to Z boson transverse momentum*, ATL-PHYS-PUB-2013-017, 2013, URL: http://cdsweb.cern.ch/record/1629317.

[13] J. Pumplin et al., *New generation of parton distributions with uncertainties from global QCD analysis*, JHEP **07** (2002) 012, arXiv: `hep-ph/0201195`.

[14] T. Sjöstrand, S. Mrenna and P. Z. Skands, *PYTHIA 6.4 Physics and Manual*, JHEP **0605** (2006) 026, arXiv: `hep-ph/0603175`.

[15] P. Z. Skands, *Tuning Monte Carlo generators: The Perugia tunes*, Phys. Rev. D **82** (7 2010) 074018, URL: `http://link.aps.org/doi/10.1103/PhysRevD.82.074018`.

[16] S. Höche et al., *QCD matrix elements and truncated showers*, JHEP **0905** (2009) 053, arXiv: `0903.1219 [hep-ph]`.

[17] T. Gleisberg and S. Höche, *Comix, a new matrix element generator*, JHEP **0812** (2008) 039, arXiv: `0808.3674 [hep-ph]`.

[18] S. Schumann and F. Krauss, *A Parton shower algorithm based on Catani-Seymour dipole factorisation*, JHEP **0803** (2008) 038, arXiv: `0709.1027 [hep-ph]`.

[19] S. Agostinelli et al., *GEANT4: A simulation toolkit*, Nucl. Instrum. Meth. **A506** (2003) 250–303.

[20] ATLAS Collaboration, *The ATLAS Simulation Infrastructure*, Eur. Phys. J. C **70** (2010) 823, arXiv: `1005.4568 [hep-ex]`.

[21] T. Gleisberg et al., *Event generation with SHERPA 1.1*, JHEP **0902** (2009) 007, arXiv: `0811.4622 [hep-ph]`.

[22] G. Corcella et al., *HERWIG 6: An Event generator for hadron emission reactions with interfering gluons (including supersymmetric processes)*, JHEP **0101** (2001) 010.

[23] E. Richter-Was, D. Froidevaux and L. Poggioli, *ATLFAST 2.0 a fast simulation package for ATLAS*, Geneva, 1998, URL: `https://cds.cern.ch/record/683751`.

[24] A. Martin et al., *Parton distributions for the LHC*, Eur.Phys.J. **C63** (2009) 189–285, arXiv: `0901.0002 [hep-ph]`.

[25] ATLAS Collaboration, *Further ATLAS tunes of PYTHIA 6 and Pythia 8*, ATL-PHYS-PUB-2011-014, 2011, URL: `http://cds.cern.ch/record/1400677`.

[26] ATLAS Collaboration, *Alignment of the ATLAS Inner Detector and its Performance in 2012*, ATLAS-CONF-2014-047, 2014, URL: `http://cdsweb.cern.ch/record/1741021`.

[27] ATLAS Collaboration, *Performance of the ATLAS Inner Detector Track and Vertex Reconstruction in High Pile-Up LHC Environment*, ATLAS-CONF-2012-042, 2012, URL: `http://cdsweb.cern.ch/record/1435196`.

[28] ATLAS Collaboration, *Charged-particle multiplicities in pp interactions at $\sqrt{s}$ = 900 GeV measured with the ATLAS detector at the LHC*, Phys. Lett. B **688** (2010) 21, arXiv: `1003.3124 [hep-ex]`.

[29] ATLAS Collaboration, *Measurement of the muon reconstruction performance of the ATLAS detector using 2011 and 2012 LHC proton–proton collision data*, Eur. Phys. J. C **74** (2014) 3130, arXiv: `1407.3935 [hep-ex]`.

[30] ATLAS Collaboration, *Electron and photon energy calibration with the ATLAS detector using LHC Run 1 data*, Eur. Phys. J. C **74** (2014) 3071, arXiv: `1407.5063 [hep-ex]`.

[31] ATLAS Collaboration, *Electron efficiency measurements with the ATLAS detector using the 2012 LHC proton–proton collision data*, ATLAS-CONF-2014-032, 2014,
URL: http://cdsweb.cern.ch/record/1706245.

[32] ATLAS Collaboration, *Measurements of the photon identification efficiency with the ATLAS detector using 4.9 fb^{-1} of pp collision data collected in 2011*, ATLAS-CONF-2012-123, 2012,
URL: http://cdsweb.cern.ch/record/1473426.

[33] ATLAS Collaboration, *Identification and energy calibration of hadronically decaying tau leptons with the ATLAS experiment in pp collisions at $\sqrt{s}$=8 TeV*, Eur. Phys. J. C **75** (2015) 303,
arXiv: 1412.7086 [hep-ex].

[34] W. Lampl et al., *Calorimeter clustering algorithms: Description and performance*, ATL-LARG-PUB-2008-002 (2008), URL: https://cds.cern.ch/record/1099735.

[35] M. Cacciari, G. P. Salam and G. Soyez, *The Anti-k(t) jet clustering algorithm*,
JHEP **0804** (2008) 063, arXiv: 0802.1189 [hep-ph].

[36] ATLAS Collaboration, *Data-driven determination of the energy scale and resolution of jets reconstructed in the ATLAS calorimeters using dijet and multijet events at $\sqrt{s} = 8\,TeV$*,
Geneva, 2015, URL: http://cds.cern.ch/record/2008678.

[37] M. Cacciari and G. P. Salam, *Pileup subtraction using jet areas*, Phys. Lett. **B659** (2008) 119–126,
arXiv: 0707.1378 [hep-ph].

[38] M. Cacciari, G. P. Salam and G. Soyez, *The Catchment Area of Jets*, JHEP **0804** (2008) 005,
arXiv: 0802.1188 [hep-ph].

[39] ATLAS Collaboration, *Tagging and suppression of pileup jets with the ATLAS detector*,
ATLAS-CONF-2014-018, 2014, URL: http://cdsweb.cern.ch/record/1700870.

[40] ATLAS Collaboration, *Pile-up subtraction and suppression for jets in ATLAS*,
ATLAS-CONF-2013-083, 2013, URL: http://cdsweb.cern.ch/record/1570994.

[41] C. Cojocaru et al., *Hadronic calibration of the ATLAS liquid argon end-cap calorimeter in the pseudorapidity region 1.6 < |eta| < 1.8 in beam tests*, Nucl.Instrum.Meth. **A531** (2004) 481–514,
arXiv: physics/0407009 [physics].

[42] ATLAS Collaboration, *Jet Calibration and Systematic Uncertainties for Jets Reconstructed in the ATLAS Detector at $\sqrt{s} = 13$ TeV*, Geneva, 2015,
URL: https://cds.cern.ch/record/2028594.

[43] ATLAS Collaboration, *Jet energy measurement and systematic uncertainties using tracks for jets and for b-quark jets produced in proton–proton collisions at $\sqrt{s} = 7$ TeV in the ATLAS detector*,
ATLAS-CONF-2013-002, 2013, URL: http://cdsweb.cern.ch/record/1504739.